INTERNATIONAL JOURNAL FOR NUMERICAL METHODS IN FLUIDS
*Int. J. Numer. Meth. Fluids* 2001; **37**: 691–719 (DOI: 10.1002/fld.192)

# The shallow flow equations solved on adaptive quadtree grids

A. G. L. Borthwick[a,*,1], S. Cruz León[a] and J. Józsa[b]

[a] *Department of Engineering Science, Oxford University, Oxford, UK*
[b] *Department of Water Resources Engineering, Technical University of Budapest, Budapest, Hungary*

## SUMMARY

This paper describes an adaptive quadtree grid-based solver of the depth-averaged shallow water equations. The model is designed to approximate flows in complicated large-scale shallow domains while focusing on important smaller-scale localized flow features. Quadtree grids are created automatically by recursive subdivision of a rectangle about discretized boundary, bathymetric or flow-related seeding points. It can be fitted in a fractal-like sense by local grid refinement to any boundary, however distorted, provided absolute convergence to the boundary is not required and a low level of stepped boundary can be tolerated. Grid information is stored as a tree data structure, with a novel indexing system used to link information on the quadtree to a finite volume discretization of the governing equations. As the flow field develops, the grids may be adapted using a parameter based on vorticity and grid cell size. The numerical model is validated using standard benchmark tests, including seiches, Coriolis-induced set-up, jet-forced flow in a circular reservoir, and wetting and drying. Wind-induced flow in the Nichupté Lagoon, México, provides an illustrative example of an application to flow in extremely complicated multi-connected regions. Copyright © 2001 John Wiley & Sons, Ltd.

KEY WORDS: computational hydraulics; quadtrees; shallow-flow hydrodynamics

## 1. INTRODUCTION

The hydrodynamics of coastal lagoons, shallow lakes, reservoirs, wide rivers and estuaries may be simulated using the depth-averaged shallow water equations. Natural flow geometries are invariably irregular and may contain significant local changes in bathymetry and bed roughness. In tidal estuaries, nearly flat bed surfaces may be subjected to periodic wetting and drying. Mixing processes in shallow flow domains can depend greatly on highly localized flow features; for example, the recirculating gyres either side of an influent stream discharging into receiving waters can act to trap pollutants.

* Correspondence to: Department of Engineering Science, University of Oxford, Parks Road, Oxford, OX1 3PJ, UK.
[1] E-mail: alistair.borthwick@eng.ox.ac.uk



*Received 24 August 1999*
*Revised 15 February 2001*

Numerical modelling of shallow flows is usually based on the two-dimensional depth-averaged shallow water equations, though progress has been made with three-dimensional solvers (e.g. Stansby and Lloyd [1]). The majority of shallow flow computational models utilize non-adaptive regular Cartesian or curvilinear meshes. However, for complicated flow geometries where local, possibly dynamically evolving, flow features are important, it is desirable for computational efficiency that the underlying meshes should be boundary fitted, automatic to generate, straightforward to refine locally, and dynamically adaptive.

Substantial research effort has been directed towards tackling the foregoing problems. Several researchers have developed patched or nested rectangular grid models of the shallow water equations. For example, Falconer and Alstead [2] used patched dynamically linked rectangular grids to provide local grid refinement in zones of interest, such as at the entrance to a tidal inlet. Rodenhuis [3] nested refined inside coarse rectangular grids. One disadvantage of patched or nested grid models is the difficulty in ensuring adequate coupling between the various mesh regions. Butler [4] applied stretched grids based on a uniformly varying distribution of straight lines to the prediction of coastal flooding. Whereas it is possible to focus on an area of interest, the refinement is not localized. Rodenhuis [3] indicates that it is hard to implement an accurate central difference scheme on stretched grids. Since Johnson's [5] WESCOR model, curvilinear mappings have become popular for boundary fitting typical shallow flow domains. Curvilinear grids may be generated by conformal, algebraic methods or by the numerical solution of the Poisson-type partial differential equations that govern the mapping [6]. Orthogonal curvilinear shallow water equation solvers have been developed which are straightforward extensions of existing rectangular grid models (e.g. Willemse *et al*. [7], Lin and Falconer [8]). Non-orthogonal curvilinear systems approaches are similar, but involve more geometric terms to permit the greater mesh flexibility. The depth-averaged velocity components may be expressed in cartesian (e.g. Johnson [5], Borthwick and Barber [9], Ye and McCorquodale [10]), covariant (e.g. Sheng and Hirsh [11]), contravariant (e.g. Borthwick and Akponasa [12]) forms leading to transformed governing equations of increasing complexity. In an alternative approach, Borthwick and Kaar [13] solved the curvilinear depth-averaged streamfunction and vorticity transport version of the shallow water equations. Scott and Barber [14] adapted non-orthogonal curvilinear meshes using weighting functions related to the flow depth for tidal flow in the Severn Estuary. Boundary fitted curvilinear shallow flow models are best suited to simple flow domains with smoothly curving boundaries, but can experience problems of mesh cell skewness leading to geometric non-conservation when applied to more complicated domains. Manually controlled block techniques are required for multiply connected domains.

Unstructured grids offer another extremely flexible approach to solving the shallow water equations in very irregular domains. Grid generation is fully automatic, and the meshes can be fitted to any geometry. There are disadvantages, notably the computational overheads due to quality checks, the lack of nodal order and the sparse form of the solution matrix. Thacker [15,16] and Bauer and Schmidt [17] solved the shallow water equations on a triangular grid by finite differences for oscillations in a shallow circular basin, and storm surges. Recently, Anastasiou and Chan [18] solved the Riemann invariant form of shallow water equations using finite volumes on an advancing front triangular grid. Unstructured grids have been widely used in finite element shallow water equation models, including those of Neta [19] and Kolar *et al*. [20].

 

This paper describes an alternative approach whereby the unsteady shallow water equations are solved on adaptive hierarchical (rectangular panel) quadtree meshes. From a computational standpoint, quadtree grid generation is economical and can be applied easily to extremely complex multiply connected geometries. There are relatively few applications of hierarchical grids to shallow flow problems, the most notable being that of Gáspár *et al*. [21], who modelled wind-induced lake circulation using the linearized shallow water equations on quadtree meshes. The work presented herein is an extension of Gáspár *et al*.'s work to the complete unsteady shallow flow equations. Of particular importance is the grid indexing system, which neatly translates information held in the quadtree data structure to conventional finite volume or finite difference notation. The shallow water equations are discretized using staggered finite volumes with a QUICKEST scheme for the non-linear momentum fluxes, and solved by an explicit time-stepping scheme. Validation results are presented for well-documented test flows, including seiche motions in a rectangular basin, jet-forced flow in a circular reservoir, a flow induced by the Coriolis force, and wetting/drying. A simulation of wind-induced flow in the Nichupté Lagoon in México illustrates the quadtree model's potential to predict the flow pattern in a complicated flow geometry.

## 2. QUADTREE GRID GENERATION

Quadtree subdivision is one of the simplest domain decomposition methods [22]. The unit square is progressively subdivided into sub-quadrants, the choice whether or not to divide dependent on interior spatial information (such as seeding points, lines, pixel colours, etc.). Quadtree techniques have been used in image processing [23], geographical information systems [22], finite element meshing [24,25], computational fluid dynamics [26,27], species transport modelling [28], and simulating steady shallow lake flows [29].

The quadtree grid generation algorithm used herein is similar to that described by Cheng *et al*. [25] and Gáspár *et al*. [28]. A root cell of unit dimension contains the normalized domain of interest. Recursive subdivision of the root cell takes place according to boundary seeding points or prescribed flow criteria. The resulting hierarchical grid has a structure that may be represented by a directed graph [28]. The original domain, $\Omega$, corresponds to the root cell. The branches indicate the subdivision process, and the subsquares $\Omega_0$, $\Omega_1$, $\Omega_2$ and $\Omega_3$, correspond to the graph nodes at the next level. The resulting direct graph is a tree-type and the leaves correspond to cells that are not subdivided further. Figure 1(a) depicts a typical 4-level quadtree grid obtained about a single seeding point. This initial grid contains large fluctuations in neighbouring cell sizes. Furthermore, hanging nodes are generated which are difficult to handle in the discretization of partial differential equations [30]. Complicated interpolation formulae are inevitably involved because careful treatment is required across cell interfaces so as not to violate conservation laws. Hence, the number of hanging nodes across any cell interface should be minimized. To ensure adequate domain definition, a regularization constraint is imposed on the grid to eliminate abrupt changes in cell size; the linear dimension of neighbour cells (faces and corners) is not permitted to differ from that of the object cell by more than a ratio of 1:2 (Figure 1(b)). It is also sensible to reduce further the number of topological arrangements of cells by additional subdivision of any large cells surrounded on

 

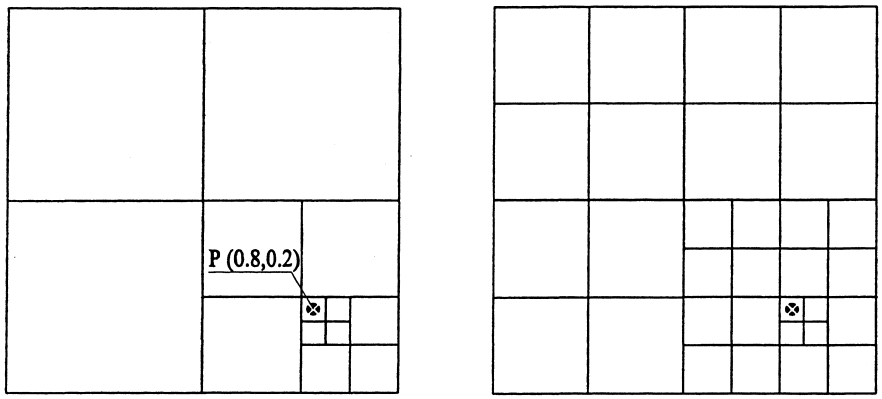


Figure 1. (a) Initial 4-level quadtree grid. (b) Regularized 4-level quadtree grid.

two or three sides by smaller cells. This has the extra benefit of reducing the local discretization errors.

A numbering system is required to identify cells and their neighbours. For example, van Dommelen and Rundensteiner [26] used a fixed length panel number in base-3 notation and Gáspár *et al.* [28] a base-4 system. The foregoing require number manipulations and tree searches when finding the neighbour cells of a given object cell. Here, a new numbering system is proposed whereby recursion is avoided and the indexing system corresponds directly to conventional finite volume or finite difference notation. This makes neighbour cell identification straightforward, unlike other quadtree numbering schemes. In the present system, each grid cell is allocated three integer numbers $(i, j, m)$ associated with row $(i)$, column $(j)$ and resolution level $(m)$ information. The row and column numbers relate to the cell location in the $x$- and $y$-directions respectively, and their values range from 0 to $n-1$ where

$$n = 2^m \tag{1}$$

Figure 2 illustrates the numbering scheme. Consider cell 11 in Figure 2(a). It has resolution level 4 and so the number of rows or columns for this level is $n = 2^4 = 16$. Hence, a 16 by 16 matrix may be constructed with each row and column numbered from 0 to $n-1 = 15$. The cell is therefore uniquely defined in this matrix at row 3 and column 12, which gives an index number (12, 3, 4) as illustrated in Figure 2(b).

The indexing system makes cell identification straightforward. For any point P $(x, y)$ inside the unit square, the cell in which it is located is determined as follows: (i) start at the highest level of resolution $m = M$, (ii) calculate $n$ from Equation (1); (iii) determine row and column integers from

 

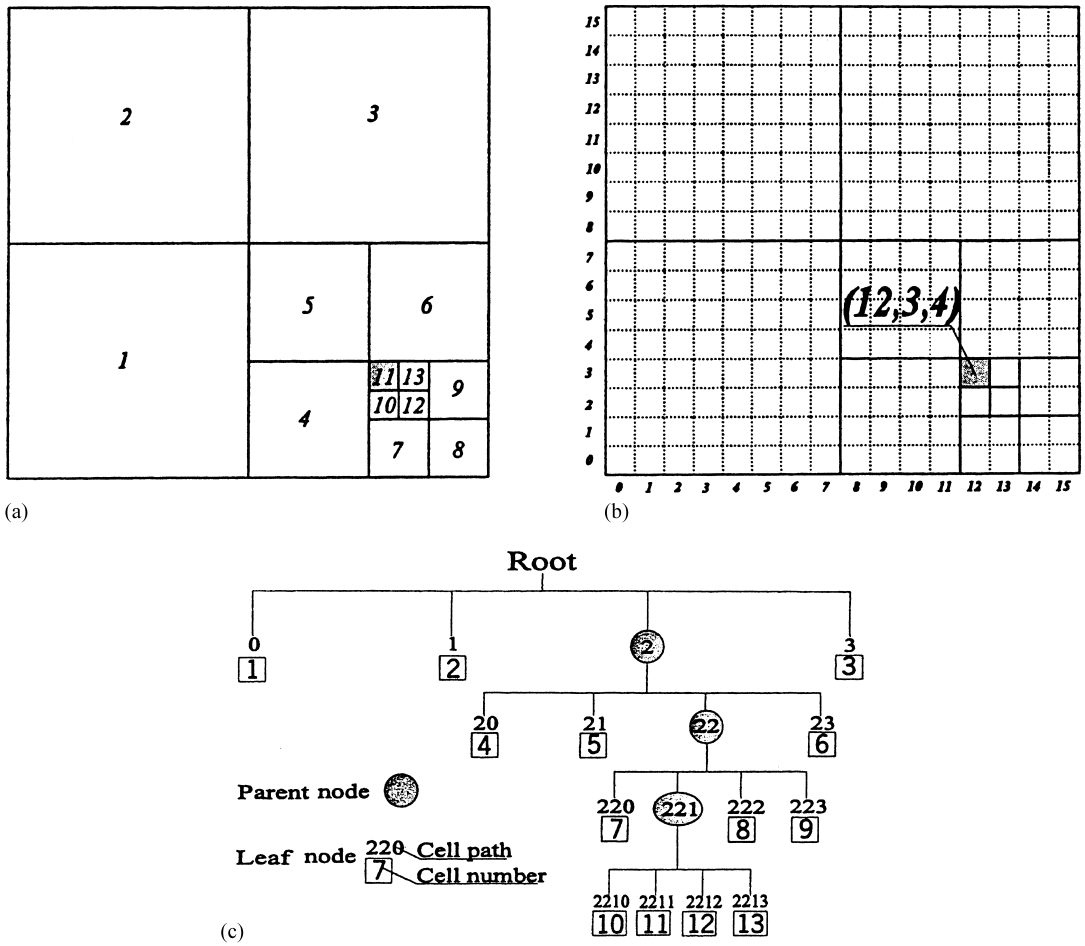


Figure 2. (a) Cell numbering for grid of Figure 1(a). (b) Indexing template for cell 11. (c). Tree representation for grid of Figure 1(a).

$$i = \mathrm{INT}[nx] \quad \text{and} \quad j = \mathrm{INT}[ny] \tag{2}$$

where INT denotes taking the integer part; (iv) compare the values of $(i, j, m)$ with those in the index list and if a match is found the cell has been identified, otherwise set $m = m - 1$ and return to (ii). As an illustrative example, consider point P (0.8, 0.2) within cell 11 in Figure 2(a). For $m = 4$, then $n = 2^4 = 16$, $i = \mathrm{INT}(16 * 0.8) = 12$ and $j = \mathrm{INT}(16 * 0.2) = 3$. This gives the cell index as (12, 3, 4).

For any arbitrary cell with index $(i, j, m)$, its linear dimension is simply

 

$$\Delta x = \Delta y = \frac{1}{2^m} \tag{3}$$

and its normalized cell lower-left corner co-ordinates are given by

$$(x_c, y_c) = (i\Delta x, j\Delta y) \tag{4}$$

For complicated boundary profiles, the boundary seeding point locations are determined using piecewise cubic–spline interpolation from an array of prescribed perimeter values. This results in fine grid resolution at the boundary even when the prescribed data are sparse. Cells that are outside the flow domain are not relevant to the flow solution and so are discarded. It is assumed that the perimeter can be represented by a polygon generated by cubic–spline interpolation. To determine whether a cell is inside or outside the polygon, it is first assumed that the left-hand edge of the unit square is outside the polygon. A horizontal line is then drawn from the object cell to the left-hand edge. The line is deemed to cross the polygon boundary whenever the $y$ co-ordinate of one end of the polygon boundary is above the line and the other end below. If the number of line crossings is even, the point is outside the polygon. If the count is odd, the point is inside. To allow for cases where the horizontal line is tangential to the polygon perimeter, the procedure is repeated using a vertical line.

The quadtree data structure is stored as a integer linked list vector, **a**. In the list, a negative number refers to an undivided leaf cell, and its absolute value is the cell number. A positive number indicates the cell is a parent, and its value points to the starting address of its four offspring. For example, the linked list, corresponding to the grid in Figure 2(a) is given in Table I, along with cell path numbers relating to the associated tree in Figure 2(c), where 0, 1, 2 and 3 refer to southwest, northwest, southeast and northeast cells relative to the parent. The cell path number is obtained directly from the cell index number $(i, j, m)$ by computing the binary array $(i_b, j_b) = \mathrm{BIN}(i, j)$ of length $m$, using additional zeros if necessary. Each pair of binary digits in the array is renumbered in sequence so that (0, 0), (0, 1), (1, 0), (1, 1) becomes 0, 1, 2, 3; the concatenated number is the cell path number. Again as an example, consider point P in Figure 2(a). Its cell index number is (12, 3, 4). The indices $i = 12$ and $j = 3$ convert to the following binary numbers $i_b = 1100$ and $j_b = 0011$, each of length $m = 4$. Thus, the cell path number is 2211.

Simple index manipulations identify the relatives of an object cell. It is important to note that the neighbour finding scheme described here is for a regularized grid. For the cell $(i, j, m)$, its parent cell index number is

Table I. Linked list for quadtree grid in Figure 2.

| $i$ | 1 | 2 | 3 | 4 | 5 | 6 | 7 | 8 | 9 | 10 | 11 | 12 | 13 | 14 | 15 | 16 |
|---|---|---|---|---|---|---|---|---|---|---|---|---|---|---|---|---|
| $a(i)$ | −1 | −2 | 5 | −3 | −4 | −5 | 9 | −6 | −7 | 13 | −8 | −9 | −10 | −11 | −12 | −13 |
| Cell path | 0 | 1 | 2 | 3 | 20 | 21 | 22 | 23 | 220 | 221 | 222 | 223 | 2210 | 2211 | 2212 | 2222 |

 

$$(i_p, j_p, m_p) = \left( \mathrm{INT}\left(\frac{i}{2}\right), \mathrm{INT}\left(\frac{j}{2}\right), m-1 \right) \tag{5}$$

and its offspring cell index numbers are

$$(i_o, j_o, m_o) \;=\; (2i + c_i, 2j + c_j, m+1) \tag{6}$$

where $(c_i, c_j) = (0, 0)$ for the southwest cell, $(c_i, c_j) = (0, 1)$ for the northwest cell, $(c_i, c_j) = (1, 0)$ for the southeast cell, and $(c_i, c_j) = (1, 1)$ for the northeast cell. For adjacent cells of the same size, the neighbour cell number $(i_n, j_n, m)$ is found by adding 1 to or subtracting 1 from the row or column of the cell index number $(i, j, m)$. For adjacent cells where the neighbour cell dimension is twice the cell size, an initial neighbour index number $(i_n, j_n, m)$ is estimated as if the cell were the same size; in this case, the tree search reveals that the cell is larger than the initial cell, and so the neighbour cell number is $(i_n/2, j_n/2, m-1)$, where the division is integer. For adjacent cells where the neighbour cell dimension is half the cell size, an initial value is again first estimated as if the cell were the same size; in this case, the tree search reveals that there is a subdivided cell with parent index number corresponding to the first estimate neighbour number $(i_n, j_n, m)$. The correct neighbour cell index number is then obtained as $(2i_n + c_i, 2j_n + c_j, m+1)$, where $c_i$ and $c_j$ control which quadrant the cell is located, as for offspring cells discussed above.

The following example illustrates the application of the quadtree grid generator. Figure 3 shows the 8-level quadtree grid generated about a circle of radius 0.3, with stems of length 0.15 and width 0.065 located diametrically opposite each other. The mesh contains 3592 cells, with 2704 cells located inside the prescribed boundary after further uniform subdivision to level 6 and 2:1 regularization. The CPU time required to generate this mesh was not significantly different to that required to generate a mesh about a simple circle without stems. Hence, an advantage of quadtree grids is their relative ease in accommodating additional mesh complexity compared with boundary fitted curvilinear meshes, which would need to be generated using block domain procedures in this case.

## 3. SHALLOW WATER EQUATIONS

The shallow water equations (see e.g. Falconer [31]) are

$$\frac{\partial \zeta}{\partial t} + \frac{\partial q_x}{\partial x} + \frac{\partial q_y}{\partial y} = 0 \tag{7}$$

$$\frac{\partial q_x}{\partial t} + \frac{\partial U q_x}{\partial x} + \frac{\partial V q_x}{\partial y} + gD\frac{\partial \zeta}{\partial x} - f_c q_y - \frac{\tau_{wx}}{\rho} + \frac{\tau_{bx}}{\rho} - \frac{1}{\rho}\frac{\partial DT_{xx}}{\partial x} - \frac{1}{\rho}\frac{\partial DT_{xy}}{\partial y} = 0 \tag{8}$$

and

 

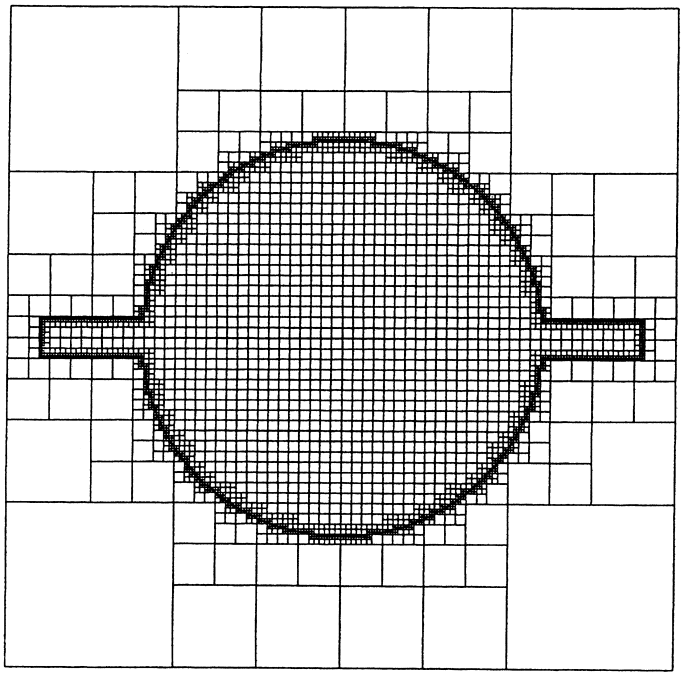

Figure 3. Quadtree grid for a circle with stems.

$$\frac{\partial q_y}{\partial t}+\frac{\partial Uq_y}{\partial x}+\frac{\partial Vq_y}{\partial y}+gD\frac{\partial \zeta}{\partial y}+f_c q_x-\frac{\tau_{wy}}{\rho}+\frac{\tau_{by}}{\rho}-\frac{1}{\rho}\frac{\partial DT_{yx}}{\partial x}-\frac{1}{\rho}\frac{\partial DT_{yy}}{\partial y}=0 \tag{9}$$

where $\zeta$ is the free surface elevation above still water level, $q_x$ and $q_y$ are volume flux components in the $x$- and $y$-directions, $f_c$ is the Coriolis parameter, $\tau_{wx}$ and $\tau_{wy}$ are wind-induced surface stress components, $\tau_{bx}$ and $\tau_{by}$ are bed stress components, $T_{xx}$, $T_{xy}$, $T_{yx}$ and $T_{yy}$ are depth-averaged effective stresses (defined later), $\rho$ is fluid density, $g$ is the acceleration due to gravity, $t$ is time and $D$ is the total depth ($D=h+\zeta$, where $h$ is the still water depth). Note that $q_x=UD$ and $q_y=VD$, where the depth-averaged velocity components are

$$U=\frac{1}{D}\int_{-h}^{\zeta}\bar{u}\,\mathrm{d}z \quad \text{and} \quad V=\frac{1}{D}\int_{-h}^{\zeta}\bar{v}\,\mathrm{d}z \tag{10}$$

in which $\bar{u}$ and $\bar{v}$ are the local mean (time-averaged) velocity components, and $z$ is measured in the vertical direction.

Wind-induced surface stresses are determined using the empirical formulae

$$\tau_{wx}=\rho_a C_w W_x\sqrt{W_x^2+W_y^2} \quad \text{and} \quad \tau_{wy}=\rho_a C_w W_y\sqrt{W_x^2+W_y^2} \tag{11}$$

 

where $C_w$ is a friction coefficient, $\rho_a$ is air density, and $W_x$ and $W_y$ are the wind velocity components. Similarly, the bed stresses are obtained from

$$\tau_{bx} = \frac{1}{2}\rho C_d U\sqrt{U^2+V^2} \quad \text{and} \quad \tau_{by} = \frac{1}{2}\rho C_d V\sqrt{U^2+V^2} \tag{12}$$

in which the bed friction coefficient $C_d = 2g/C^2 = 2n^2 g/R^{1/3}$, where $R$ is the hydraulic radius and $C$ and $n$ are the Chézy and Manning coefficients respectively.

To enable finite volume discretizations, the shallow water equations are rewritten in flux form, using Cartesian tensor notation, as

$$\frac{\partial \zeta}{\partial t} + \frac{\partial q_i}{\partial x_i} = 0 \tag{13}$$

and

$$\frac{\partial q_i}{\partial t} + \frac{\partial J_{ij}}{\partial x_j} + gD\frac{\partial \zeta}{\partial x_i} + S_i = 0 \tag{14}$$

in which $x_i$ is the co-ordinate direction (where $i=1$ refers to the $x$-direction and $i=2$ refers to the $y$-direction), $q_i = U_i D$ is the flux component corresponding to the depth-averaged velocity component $U_i$. The source term $S_i$ is

$$S_i = \epsilon_{ij} f_c q_j - \frac{\tau_{wi}}{\rho} + \frac{\tau_{bi}}{\rho} \tag{15}$$

where $\tau_{wi}$ is a surface stress component, $\tau_{bi}$ is a bed stress component, the permutation tensor $\epsilon_{ij} = -1$ if $i, j = 1, 2$; $\epsilon_{ij} = 1$ if $i, j = 2, 1$ and $\epsilon_{ij} = 0$ if $i = j$. Also

$$J_{ij} = U_j q_i - \frac{D}{p} T_{ij} \tag{16}$$

The depth-averaged effective stress, $T_{ij}$, comprises the sum of molecular diffusion, Reynolds and dispersion stresses

$$T_{ij} = \frac{1}{D}\int_{-h}^{\zeta} \rho v\left(\frac{\partial \bar{u}_i}{\partial x_j} + \frac{\partial \bar{u}_j}{\partial x_i}\right) \mathrm{d}z - \frac{1}{D}\int_{-h}^{\zeta} \rho\overline{u_i u_j}\,\mathrm{d}z - \frac{1}{D}\int_{-h}^{\zeta} \rho(\bar{u}_i - U_i)(\bar{u}_j - U_j)\,\mathrm{d}z \tag{17}$$

where $v$ is the kinematic viscosity coefficient of water. In turbulent flows, molecular diffusion is of much smaller magnitude than the Reynolds stresses, and so can be neglected. Using the Boussinesq approximation to relate the Reynolds stresses to the depth-averaged velocity gradients, and ignoring the cross-derivative terms

 

$$-\frac{1}{D}\int_{-h}^{\zeta}\rho\,\overline{u_i u_j}\,\mathrm{d}z=\frac{\rho\tilde{\nu}_\mathrm{t}}{D}\frac{\partial q_i}{\partial x_j} \tag{18}$$

where $\tilde{\nu}_\mathrm{t}$ is the depth-averaged kinematic eddy viscosity coefficient. The dispersion term results from depth-integration of the advection terms and may be evaluated for prescribed velocity distributions to give (e.g. Falconer [31])

$$\frac{1}{D}\int_{-h}^{\zeta}\rho(\bar{u}_i-U_i)(\bar{u}_j-U_j)\,\mathrm{d}z=\frac{\rho}{D}(\beta-1)U_j q_i \tag{19}$$

The $\beta$ coefficient takes its value depending on the assumed vertical velocity profile. For example, $\beta=1+C_\mathrm{f}/\kappa^2$ for a logarithmic profile [31], where $\kappa$ is the von Kármán constant. Hence, the depth-averaged effective stress is

$$T_{ij}=\frac{\rho\tilde{\nu}_\mathrm{t}}{D}\frac{\partial q_i}{\partial x_j}-\frac{\rho}{D}(\beta-1)U_j q_i \tag{20}$$

and the flux term is written

$$J_{ij}=\beta U_j q_i-\tilde{\nu}_\mathrm{t}\frac{\partial q_i}{\partial x_j} \tag{21}$$

The flux form of the shallow water equations is therefore expressed by Equations (13)–(15) and (21).

## 4. NUMERICAL SCHEME

The shallow water equations are spatially discretized using staggered control volumes. The continuity equation (13) is integrated over each grid cell, whereas the momentum equations (14) are integrated over adjacent half-cells about the flux interface. It should be noted that in a staggered hierarchical grid not all of the variables ($\zeta$, $q_x$, $q_y$) are located at the required position in the control volumes; instead these values have to be interpolated from nearby nodal values [32]. Here, interpolation has been used with the assumption that the grid may be refined at the relevant cell should more precise values be required, so that the grid resolution will match the quality of the data.

Figure 4 illustrates the control volume for the continuity equation. The control volume may have a maximum of six face neighbours ($N_1,\ldots,N_6$) depending on the arrangement of neighbouring cells. The labelling system is such that the water level node is located at the cell-centre, $\zeta_\mathrm{c}=\zeta_{i,j,m}$, the $x$-direction volume flux at the west face of the cell, $q_{x\mathrm{w}}=[q_x]_{i,j,m}$, and the $y$-direction volume flux at the south face, $q_{y\mathrm{s}}=[q_y]_{i,j,m}$. Integration of the continuity equation (13) over the control volume gives

 

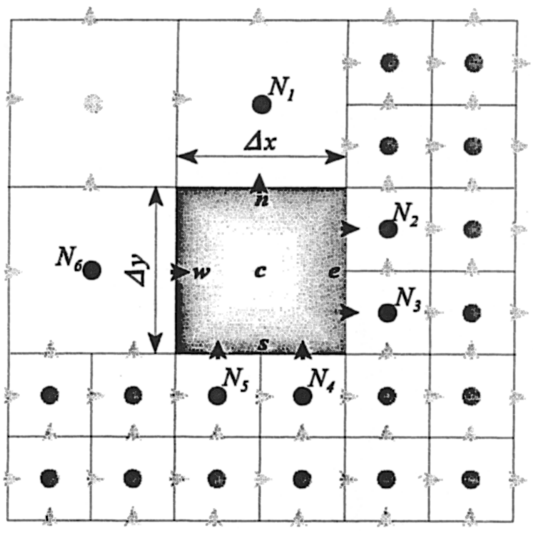


Figure 4. Control volume for the continuity equation.

$$\int_t^{t+\Delta t}\int_A \frac{\partial \zeta}{\partial t}\,\mathrm{d}A\,\mathrm{d}t + \int_t^{t+\Delta t}\int_A \frac{\partial q_i}{\partial x_i}\,\mathrm{d}A\,\mathrm{d}t = 0 \tag{22}$$

where $A = \Delta x \Delta y$ is the control volume area. Taking the water level $\zeta$ to be the average over the control volume, integrating the first term over the area, integrating the second (flux gradient) term in time after applying Green's theorem, and rearranging gives

$$\zeta_{\mathrm{c}}^{n+1} - \zeta_{\mathrm{c}}^{n} + \frac{1}{\Delta x}(Q_{\mathrm{e}} - Q_{\mathrm{w}}) + \frac{1}{\Delta y}(Q_{\mathrm{n}} - Q_{\mathrm{s}}) = 0 \tag{23}$$

in which

$$Q_{\mathrm{e}} = \frac{1}{s}\sum_{k=1}^{s}\left[\int_t^{t+\Delta t}(q_x)_{\mathrm{e}}\right]_k \mathrm{d}t \simeq \theta\frac{\Delta t}{s}\sum_{k=1}^{s}[(q_x)_{\mathrm{e}}^{n+1}]_k + (1-\theta)\frac{\Delta t}{s}\sum_{k=1}^{s}[(q_x)_{\mathrm{e}}^{n}]_k \tag{24}$$

$$Q_{\mathrm{n}} = \frac{1}{s}\sum_{k=1}^{s}\left[\int_t^{t+\Delta t}(q_y)_{\mathrm{n}}\right]_k \mathrm{d}t \simeq \theta\frac{\Delta t}{s}\sum_{k=1}^{s}[(q_y)_{\mathrm{n}}^{n+1}]_k + (1-\theta)\frac{\Delta t}{s}\sum_{k=1}^{s}[(q_y)_{\mathrm{n}}^{n}]_k \tag{25}$$

$$Q_{\mathrm{w}} = \frac{1}{s}\sum_{k=1}^{s}\left[\int_t^{t+\Delta t}(q_x)_{\mathrm{w}}\right]_k \mathrm{d}t \simeq \theta\frac{\Delta t}{s}\sum_{k=1}^{s}[(q_x)_{\mathrm{w}}^{n+1}]_k + (1-\theta)\frac{\Delta t}{s}\sum_{k=1}^{s}[(q_x)_{\mathrm{w}}^{n}]_k \tag{26}$$

and

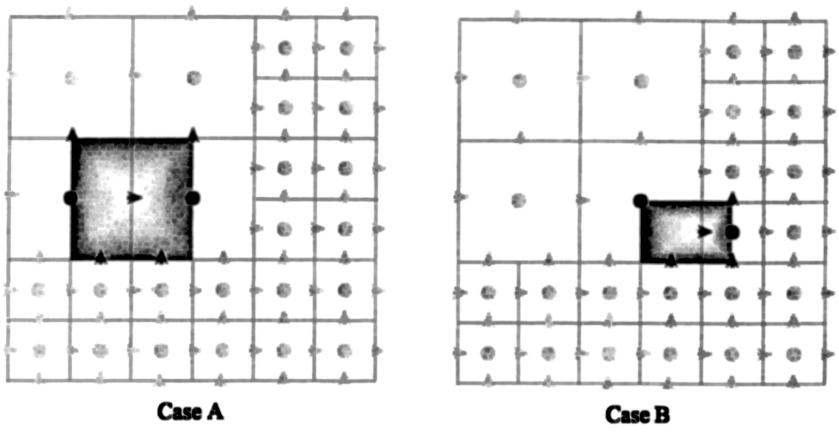


Figure 5. Control volume for the $x$-momentum equation.

$$Q_s = \frac{1}{s}\sum_{k=1}^{s}\left[\int_t^{t+\Delta t}(q_y)_s\right]_k \mathrm{d}t \simeq \theta\frac{\Delta t}{s}\sum_{k=1}^{s}[(q_y)_s^{n+1}]_k + (1-\theta)\frac{\Delta t}{s}\sum_{k=1}^{s}[(q_y)_s^n]_k \tag{27}$$

where $s$ is the number of discharges (1 or 2) through the control volume face (Figure 4) and $\theta$ is a weighting factor, $0 \le \theta \le 1$. The scheme is explicit for $\theta = 0$, otherwise it is implicit.

Integration of the $x$-momentum equation over the control volume in Figure 5 gives

$$\int_t^{t+\Delta t}\int_A \frac{\partial q_i}{\partial t}\,\mathrm{d}A\,\mathrm{d}t + \int_t^{t+\Delta t}\int_A \frac{\partial J_{ij}}{\partial x_j}\,\mathrm{d}A\,\mathrm{d}t + \int_t^{t+\Delta t}\int_A gD\frac{\partial \zeta}{\partial x_i}\,\mathrm{d}A\,\mathrm{d}t + \int_t^{t+\Delta t}\int_A S_i\,\mathrm{d}A\,\mathrm{d}t = 0 \tag{28}$$

Taking the flux $q_i$ to be the average over the control volume and evaluating the integrals, the discretized $x$-momentum equation is

$$\begin{aligned}&(q_x)_c^{n+1} - (q_x)_c^n + \frac{\theta\Delta t}{\Delta x}[(J_{xx})_e^{n+1} - (J_{xx})_w^{n+1}] + \frac{(1-\theta)\Delta t}{\Delta x}[(J_{xx})_e^n - (J_{xx})_w^n]\\ &+ \frac{\theta\Delta t}{\Delta y}[(J_{xy})_n^{n+1} - (J_{xy})_s^{n+1}] + \frac{(1-\theta)\Delta t}{\Delta y}[(J_{xy})_n^n - (J_{xy})_s^n] + \frac{\theta\Delta t}{\Delta x}gD[\zeta_e^{n+1} - \zeta_w^{n+1}]\\ &+ \frac{(1-\theta)\Delta t}{\Delta x}gD[\zeta_e^n - \zeta_w^n] + \theta\Delta t S_x^{n+1} + (1-\theta)\Delta t S_x^n = 0\end{aligned} \tag{29}$$

Similarly, the discretized $y$-momentum equation is

 

$$(q_y)_c^{n+1} - (q_y)_c^n + \frac{\theta \Delta t}{\Delta x}[(J_{yx})_e^{n+1} - (J_{yx})_w^{n+1}] + \frac{(1-\theta)\Delta t}{\Delta x}[(J_{yx})_e^n - (J_{yx})_w^n]$$
$$+ \frac{\theta \Delta t}{\Delta y}[(J_{yy})_n^{n+1} - (J_{yy})_s^{n+1}] + \frac{(1-\theta)\Delta t}{\Delta y}[(J_{yy})_n^n - (J_{yy})_s^n] + \frac{\theta \Delta t}{\Delta y} gD[\zeta_n^{n+1} - \zeta_s^{n+1}]$$
$$+ \frac{(1-\theta)\Delta t}{\Delta y} gD[\zeta_n^n - \zeta_s^n] + \theta \Delta t S_y^{n+1} + (1-\theta)\Delta t S_y^n = 0 \tag{30}$$

When implemented on the regularized quadtree grid, the approximations to the momentum equations may require interpolated values of variables at locations other than computational nodes depending on the local grid configuration. The variables in the continuity equation do not require interpolation because, by definition, the fluxes are located at the faces of the control volume and the water level at its centre. The water level in the $x$-momentum control volume depicted in Case A (Figure 5) does not require interpolation. Linear $h$-interpolation is used to estimate the water level at the face centre of the $x$-momentum control volume in Case B (Figure 5). For the regularized quadtree grid, the two cases shown in Figure 6 correspond to all possible local cell configurations after rotation. The interpolated value, $h_0$, is given for the case in Figure 6(a) by

$$h_0 = \frac{1}{2} h_2 + \frac{1}{4}(h_1 + h_3) \tag{31}$$

and for the case in Figure 6(b) by

$$h_0 = \frac{1}{3} h_1 + \frac{1}{2} h_2 + \frac{1}{6} h_3 \tag{32}$$

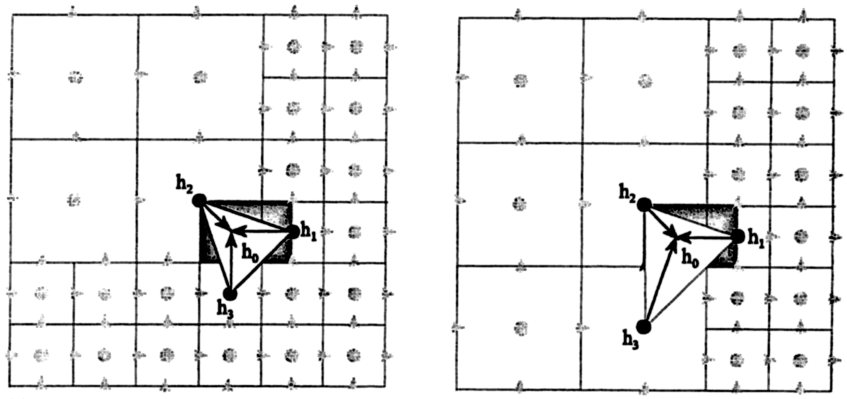


Figure 6. Water level interpolations.

 

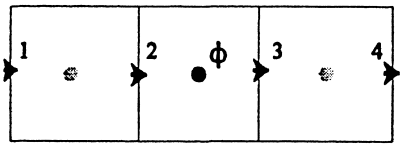


Figure 7. $\phi$ position at cell centre.

Where $h_3$ does not exist (for example, at a solid boundary), the value of $h_0$ is estimated from

$$h_0 = \frac{1}{3}h_1 + \frac{2}{3}h_2 \tag{33}$$

The total momentum flux, $J_{ij}$, is also calculated at the face centres of the momentum control volume by interpolation. To aid dealing with the local cell configurations, an auxiliary variable, $\phi$, is specified at the cell centre, corresponding to the $\zeta$-position (see Figure 7). The auxiliary variable is defined as follows:

if $U_2 \geq 0$

$$\phi = U_2(q_x)_2 + \frac{(1+\gamma)}{4}[U_3(q_x)_3 - U_2(q_x)_2] + \frac{(1-\gamma)}{4}[U_2(q_x)_2 - U_1(q_x)_1] \tag{34}$$

if $U_2 < 0$

$$\phi = U_3(q_x)_3 + \frac{(1+\gamma)}{4}[U_2(q_x)_2 - U_3(q_x)_3] + \frac{(1-\gamma)}{4}[U_3(q_x)_3 - U_4(q_x)_4] \tag{35}$$

where $\gamma$ is a parameter in the range $[-1, 1]$. This $\gamma$-interpolation [33] is second-order accurate when applied on a regular grid. For $\gamma = -1$, it gives a fully one-sided upwind scheme on a regular grid; for $\gamma = 1$, it gives a second-order central scheme; for $\gamma = 0$, it gives Fromm's method; for $\gamma = \frac{1}{3}$, it gives the QUICKEST scheme. Now the interpolation problem has been reduced to finding values of $U$ and $q_x$ at positions 1, 2, 3 and 4 in Figure 8. The total momentum flux at the momentum control volume face is

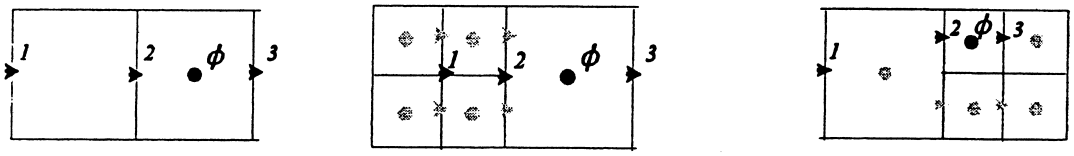


Figure 8. Basic topologies for $\phi$ interpolation.

 

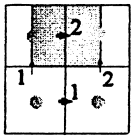


Figure 9. Linear interpolation for $(J_{xy})_s$.

$$J_{xx} = \beta\phi - \hat{v}_t\left(\frac{(q_x)_3 - (q_x)_2}{\Delta x}\right) \tag{36}$$

and, if necessary, $J_{xx}$ can be found by an $h$-interpolation (taking $h$ as $J_{xx}$). On the other hand, the cross-advective terms (e.g. $J_{xy}$) may be evaluated at the faces of the control volume by linear interpolation. For example, $(J_{xy})_s$ in Figure 9 is determined from

$$(J_{xy})_s = \frac{1}{4}\beta(V_1 + V_2)[(q_x)_1 + (q_x)_2] - \hat{v}_t\left(\frac{(q_x)_2 - (q_x)_1}{\Delta y}\right) \tag{37}$$

In the present work, Dirichlet conditions were implemented at all boundaries. Closed boundaries are located at volume flux, $q_x$ or $q_y$, positions and may be slip or no-slip as specified. Open boundaries are restricted to subcritical flows. At an inflow boundary two conditions are prescribed: the value of water level or discharge as a function of time; and the flow direction fixed as either $x$ or $y$. At an outflow boundary, the water level or discharge is specified as a function of time.

Grid adaptation may be achieved using local mesh enrichment and coarsening controlled by a parameter determined from a suitable flow variable multiplied by the local grid size. For shear flows, the depth-averaged vorticity and cell area are sensible choices of flow variable and local grid size respectively. Hence, the control parameter is the grid cell circulation defined as

$$\Delta\Gamma = \left(\frac{\partial V}{\partial x} - \frac{\partial U}{\partial y}\right)\Delta x \Delta y \tag{38}$$

In the present implementation, $\Delta\Gamma$ is kept reasonably constant as the flow field develops by refining the grid size in areas where the depth-averaged vorticity is high.

Numerical solution of the discretized shallow water equations was undertaken using an explicit time-stepping scheme with $\theta = 0$ and $\gamma = \frac{1}{3}$. The procedure may be summarized as follows:

(i) Create initial quadtree mesh and initialize flow variables;
(ii) Update water levels $\zeta$ at each cell using Equation (23);
(iii) Calculate new depth values, $D = h + \zeta$;
(iv) Prescribe updated open boundary water levels;
(v) Calculate new fluxes $q_x$ and $q_y$ using Equations (29) and (30);
(vi) Update open boundary cell discharges;

 

(vii) Increment by one time step;
(viii) Adapt the grid, if required;
(ix) Return to step (ii), until simulation is completed.

Note that three arrays of flags, one for each variable ($\zeta$, $q_x$, $q_y$), express whether the point is wet or dry.

To achieve stability, the time step in the explicit scheme was set at a value sufficiently small that it satisfied the conventional Courant–Friedrichs–Lewy (CFL) stability criterion

$$\Delta t \leq \frac{C_r \min\{\Delta x, \Delta y\}}{S_{\max}} \tag{39}$$

where the CFL number $C_r = 0.8$ and the maximum wave speed in the entire flow domain may be estimated from

$$S_{\max} = \max\{\ |U_c^n| + \sqrt{gd_c},\ |V_c^n| + \sqrt{gd_c}\} \tag{40}$$

It should be noted that, although the criterion gave satisfactory results for the cases considered herein, Fraccorollo and Toro [34] have found that the simple CFL criterion leads to poor estimates of shock-like free surface flows, such as the initial evolution of dam break fronts, particularly over dry beds. Fraccorollo and Toro propose an improved CFL-type criterion in such cases.

## 5. RESULTS

The numerical model was validated using various benchmark tests, including seiching in a rectangular basin and jet-forced flow in a circular basin. The tests give a fairly comprehensive indication of the model's performance, and close agreement is achieved in comparison with alternative theoretical models. After validation, the model was used to simulate wind-induced flow in the Nichupté Lagoon, México.

### *5.1. Seiche motions without bed friction*

Consider the seiching motions in a rectangular basin of length $L_x$, width $L_y$ and uniform still water depth $d$. In the absence of Coriolis and shear stress terms, the shallow water equations for a horizontal-bottomed basin may be solved to give the free surface amplitude as

$$\zeta(x, y, t) = \frac{H}{2} \cos(k_x x) \cos(k_y y)\, e^{i\omega t} \tag{41}$$

where $i = \sqrt{-1}$, the initial wave height is $H$, the wave numbers are $k_x = n_x \pi / L_x$ and $k_y = n_y \pi / L_y$, and $n_x$, $n_y$ are integers representing the number of half-wavelengths in the $x$- and $y$-directions respectively. The seiche period is given by

 

$$T = \frac{2}{\sqrt{gd\left(\frac{n_x^2}{L_x^2} + \frac{n_y^2}{L_y^2}\right)}} \tag{42}$$

For the validation test, $L_x = 10000$ m, $L_y = 5000$ m and $d = 1$ m. The wind speed is 10 m s$^{-1}$ from the west, and the wind drag coefficient is 0.002. There is no bed friction, no viscosity and no Coriolis force. The computational quadtree grid is illustrated in Figure 10; the grid has maximum resolution level 7, and minimum level 6. The unsteady model was run until steady state was reached, giving a set-up of approximately 0.1 m; the wind speed was then set to zero (the initial condition) and the model run for a further 50000 s (13.88 h). Figure 11 shows the simulated and analytical water level variations predicted at the east end of the basin. After several cycles, a slight reduction in amplitude occurs indicating that the scheme experiences some artificial diffusion.

It should be noted that a test with frictional damping was also carried out, and reasonable agreement obtained with an analytical solution.

### 5.2. *Coriolis-induced flow*

For a unidirectional steady flow such that the momentum flux $q_y = 0$ and water level gradient in the $x$-direction $\partial\zeta/\partial x = 0$, in the presence of the Coriolis force, but without bed and surface stresses, the $y$-momentum equation reduces to

$$\frac{\partial\zeta}{\partial y} = -\frac{f_c q_x}{gD} \tag{43}$$

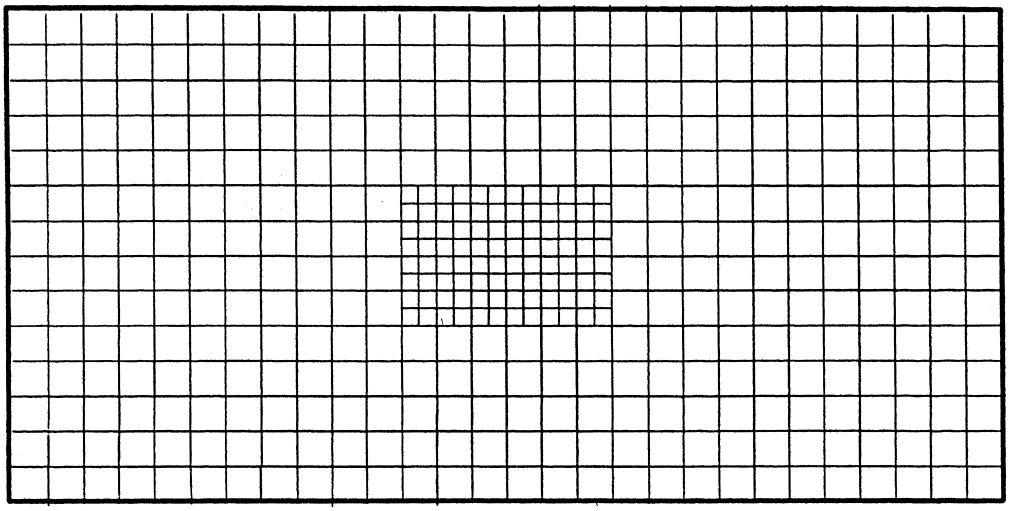

Figure 10. Quadtree grid used for seiching tests.

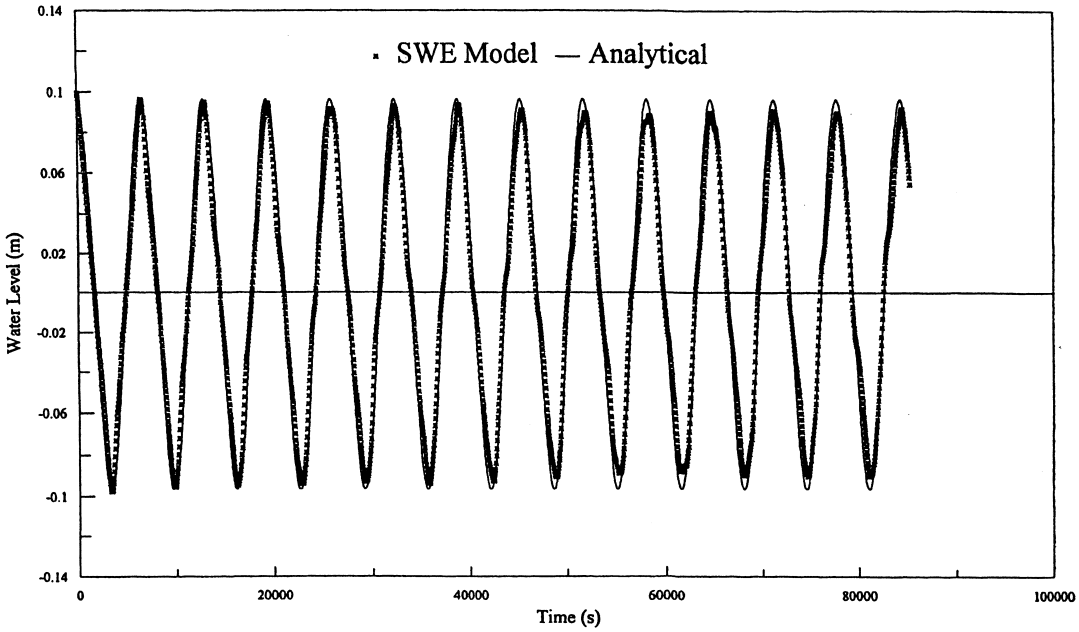


Figure 11. Water level motions for seiche without frictional damping.

Hence, in the case of uniform velocity, the Coriolis effect causes a water level gradient perpendicular to the flow direction. The grid depicted in Figure 12 covers a 400 km$^2$ square region, and consists of 20 by 20 cells each 1000 m in length. A uniform discharge of $q_x = 10$ m$^2$ s$^{-1}$, a uniform still water depth of 10 m, and Coriolis parameter $f_c = 1.205 \times 10^{-4}$ were prescribed. From Equation (43), a water level gradient of $\partial\zeta/\partial y = -0.123 \times 10^{-4}$ m m$^{-1}$ is predicted; and so the water level on the northern boundary should be 0.246 m above the southern boundary. Figure 13 illustrates the water level distribution, which is in excellent agreement with the analytical solution.

### 5.3. *Jet-forced flow in a circular reservoir*

The circular basin has a diameter of 1.5 m, a uniform still water depth of 0.1 m, and symmetric inlet and outlet stems of width $b = 0.156$ m. Laminar jet-forced flow in a circular basin is useful in testing the momentum diffusion and advective terms in the shallow water equations, in that large vorticity gradients are generated near the interior corners of the inflow and outflow stems. The inlet Reynolds number is defined as

$$Re = \frac{bU}{2\nu} \tag{44}$$

 

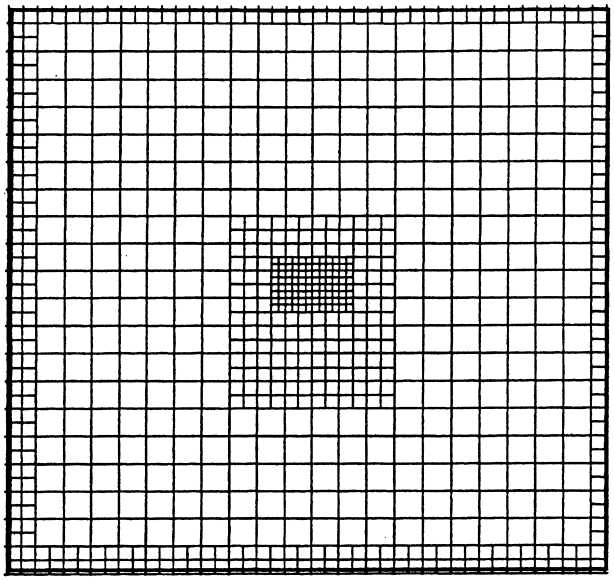

Figure 12. Grid used for Coriolis test.

where $U$ is the inlet velocity and $v$ is the fluid kinematic viscosity. Here, $U = 0.1$ m s$^{-1}$ and $v = 0.00078$ m$^2$ s$^{-1}$, giving an inlet Reynolds number $Re = 10$. The initial quadtree grid, illustrated in Figure 14, is subdivided to level 8 at the circular boundary ($\Delta x = 0.01$ m) with an interior regular grid of level 5. Bed and surface stresses are set to zero, along with the Coriolis parameter. During the time stepped flow simulation the grid was refined according to the local cell circulation criterion, Equation (38), up to level 10. Figure 15 depicts the converged grid at steady state. The velocity vector distribution is given in Figure 16, where increased resolution is evident at the shear layers close to the inlet and outlet. The overall flow pattern is in close agreement with Dennis [38] who obtained a semi-analytical solution to the two-dimensional flow problem and numerical predictions by Borthwick and Kaar [13] who solved the shallow water equations in curvilinear depth-averaged stream function and vorticity transport form on a boundary-fitted grid.

### *5.4. Wetting and drying tests*

In the present model, wetting and drying is implemented using a simple mass conservation approach designed for the explicit scheme on a staggered quadtree grid. The water depth in each cell is checked, and the cell is considered to be wet if the depth is greater than a prescribed minimum value (5 cm in the cases considered in this paper). It should be noted that the minimum depth criterion has an effect on the bed shear stress term, as the depth appears in the denominator. If the depth estimated at a cell face is less than the prescribed minimum, then the momentum flux is set to zero there. When the depth is greater than the minimum, the

 

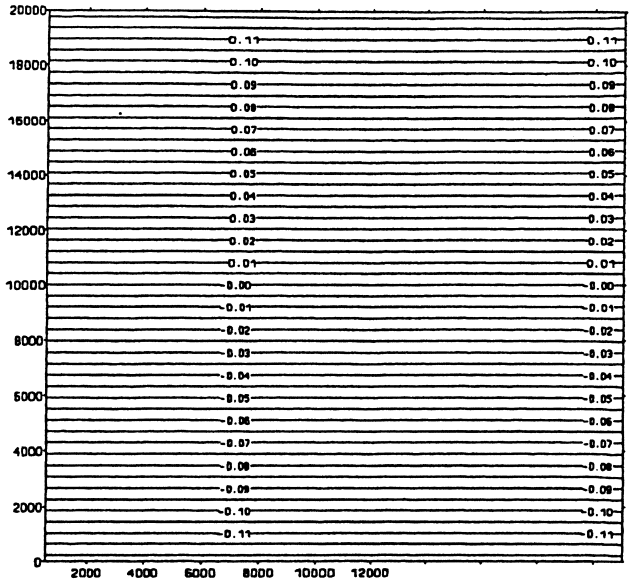


Figure 13. Water level contours for the Coriolis test.

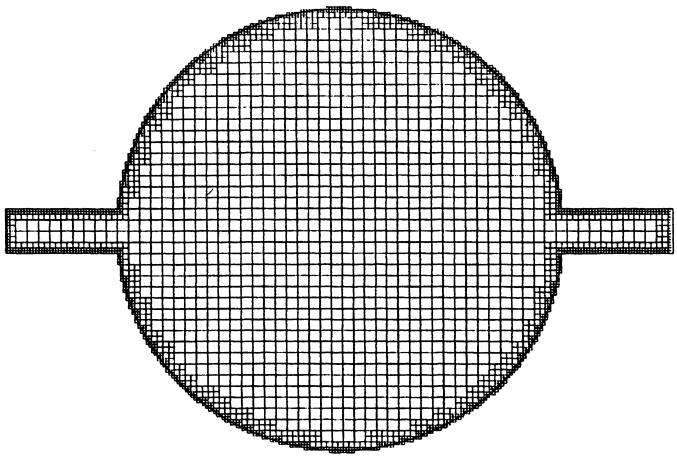

Figure 14. Initial quadtree grid for jet-forced flow in a circular reservoir.

 

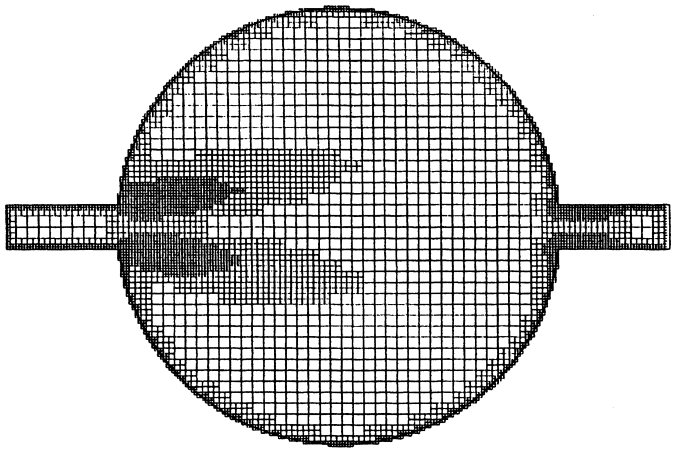

Figure 15. Adapted quadtree grid for jet-forced flow in a circular reservoir.

momentum flux is evaluated using the appropriate momentum equation. For the cases considered herein, the scheme did not produce non-physical oscillations.

Three standard test cases were implemented. In the first, oscillatory wetting and drying were simulated in a rectangular basin containing a plane sloping beach. The second test comprised tidal flow around a gently sloping circular island. In both cases, the wetting and drying

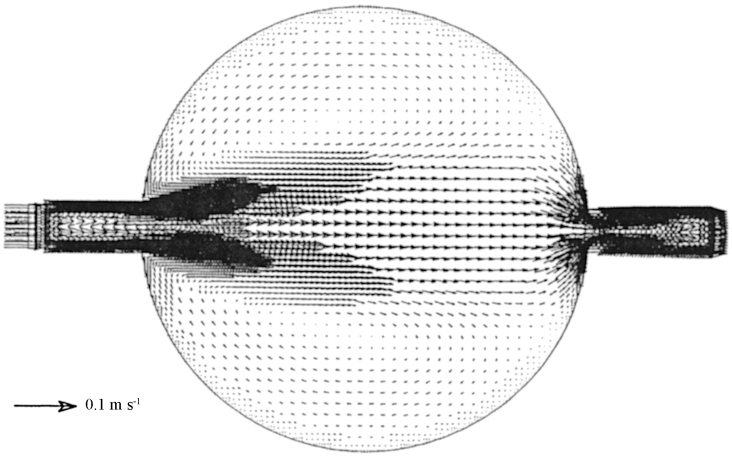


Figure 16. Depth-averaged velocity vectors in circular reservoir, $Re = 10$.

 

simulations gave satisfactory results, with the shoreline moving as expected (see Cruz León [35]). It should be underlined that the wetting and drying model used herein is very simple and could suffer instabilities in the drying phase due to feedback from instantaneous flux changes at cell boundaries (see Falconer and Owens [36]). More advanced, and physically correct, wetting and drying approaches such as that proposed by Falconer and Chen [37] are recommended for site-specific practical applications.

The third, which is described in detail here, focused on inundation and involved a comparison with Thacker's [16] exact solution of the non-linear shallow water equations for a parabolic mound of water spreading over a frictionless horizontal bed. There is no Coriolis force. The free surface elevation and $x$- and $y$-direction mass fluxes are

$$\zeta = h_0\left[\frac{T^2}{t^2+T^2} - \frac{x^2+y^2}{R_0^2}\left(\frac{T^2}{t^2+T^2}\right)^2\right] \tag{45}$$

$$q_x = \frac{xt\zeta}{t^2+T^2} \quad \text{and} \quad q_y = \frac{yt\zeta}{t^2+T^2} \tag{46}$$

where $h_0$ is the initial free surface elevation of the centre of the parabolic mound above the horizontal bed, $x$ and $y$ are the horizontal Cartesian co-ordinates measured from the mound centre, and $T$ is given by

$$T = \frac{R_0}{(2gh_0)^{1/2}} \tag{47}$$

in which $R_0$ is the initial radius of the mound. For initial conditions, $q_x = q_y = 0$ at $t = 0$, Equation (45) becomes

$$\zeta = h_0\left[1 - \frac{x^2+y^2}{R_0^2}\right] \tag{48}$$

At time $t = T$, the central water height is $h_0/2$. In this case, the following parameters are used: initial water height, $h_0 = 1$ m; initial radius $R_0 = 250$ m. The computational grid, in Figure 17, has two levels of refinement: level 6 and level 7, the latter with $\Delta x = 7.8125$ m. The refined zone is non-adaptive and has been deliberately selected because it does not fit the expected polar evolution of the flood. Figure 18 presents the predicted water level contours at $t = T$, which compare well with the analytical solution given in Figure 19, even though the grid is quite coarse. The results demonstrate that the inundation front remains quite circular, even when propagating through quadtree grid zones of different resolution. This confirms that the finite volume solution of the wetting problem is proper in that it does not produce significant amplitude or phase errors. The test is also valid for mass and momentum conservation.

 

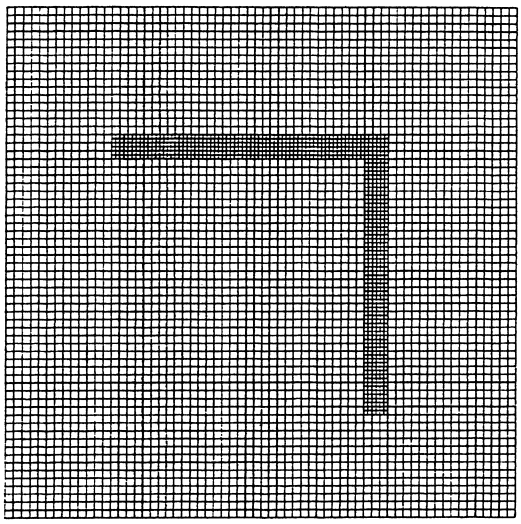

Figure 17. Quadtree grid used in parabolic mound test.

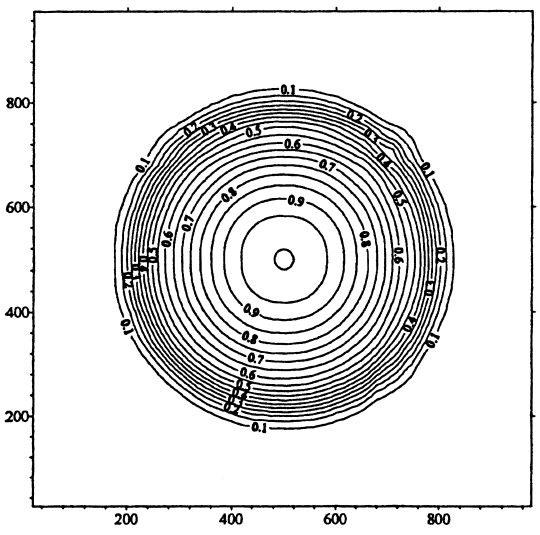


Figure 18. Simulated water level contours for circular mound at $t = T$.

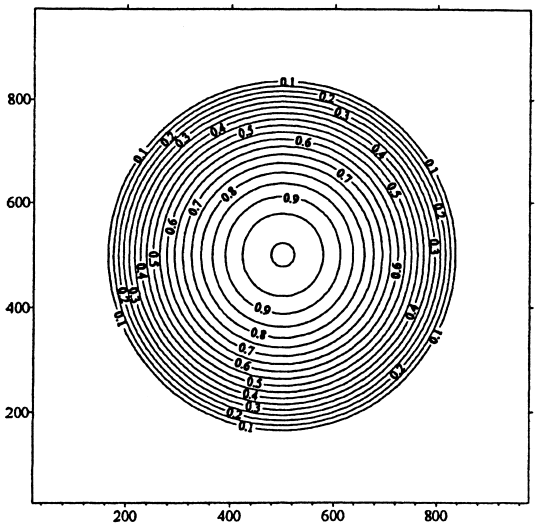


Figure 19. Analytical water level contours for circular mound at $t = T$.

### 5.5. Wind-induced circulation in the Nichupté Lagoon

In Mexico there are more than 128 coastal lagoons, all sharing certain common features, namely: shallow water; complicated geometry; high nutrient levels; large seasonal variations in temperature and salinity; erodible beds; fresh water inflows; and connections to the sea. A lack of understanding of the behaviour of these shallow water ecosystems has led to damaging management strategies being adopted locally. For example, the aquatic environment of the Laguna de Términos was destabilized by widening one of its entrances to the sea. In the Laguna de Nichupté, eutrophication resulted from partial closure of its entrance. Significant reductions in fish populations have been caused by the discharge of organic material by riparian owners. Hence, there is a major incentive to predict accurately the behaviour of coastal lagoon ecosystems.

The Nichupté Lagoon is situated in the south-east of México. It is approximately 13 km long and 6 km wide (Figure 20) with a surface area of 48 km$^2$ and a volume of $90 \times 10^6$ m$^3$. The water depths are extremely shallow, having an average of 2 m, and ranging from a few centimetres to 5 m in one of the channels.

Figure 21 illustrates the 12-level quadtree grid (superimposed on a 6-level uniform grid) created about seeding points which describe the flow boundaries of the Nichupté Lagoon. The portion of grid located within the Lagoon geometry has 1:2 regularization, whereas that outside the Lagoon is left non-regularized. The grid achieves high resolution in regions where the geometry is contorted, but with a manageable total of 8125 interior cells. It should be noted that the quadtree grid cells vary in length from 218 m at level 6 to 3.4 m at level 12. It is evident that the mesh has high resolution in regions where the geometry is particularly contorted, whilst the total number of grid cells is much lower than would be required for a

 

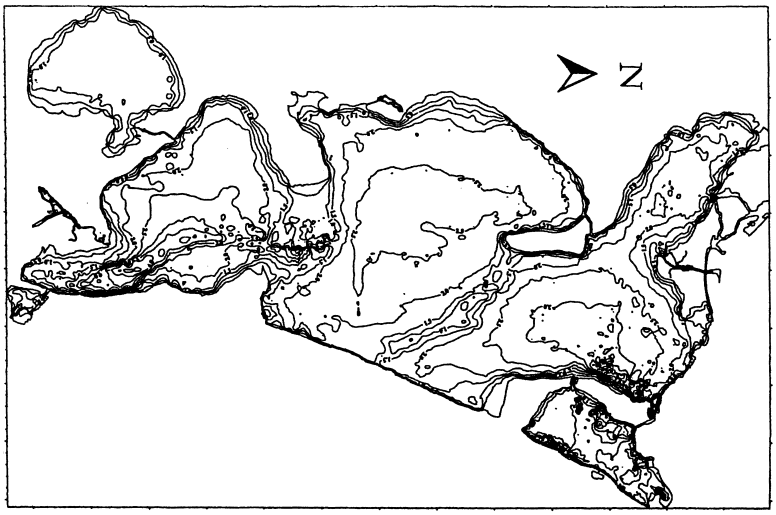


Figure 20. Nichupté Lagoon bathymetry.

uniformly fine grid. In this case, the quadtree grid technique is more effective than curvilinear or regular patched grid generation methods, which have to account for interface information in the resulting block meshes. The quadtree grid gives fine resolution at the point where the channel narrows, which is obviously useful for accurate flow modelling. Figure 22 shows a snapshot of the wind-induced flow during the initial set-up for a prevailing wind of speed 10 m $s^{-1}$, using the quadtree shallow water solver, with uniform surface roughness coefficient $C_w = 0.002$. Bed roughness is assumed constant throughout the lagoon corresponding to a Chézy coefficient of 50 $m^{1/2}$ $s^{-1}$. The largest depth-averaged velocities occur in the channels connecting the lagoon system and in the shallows close to headlands. These transient currents play a vital role in the water exchange mechanism between adjacent lagoons. Quadtree gridding is thus very useful in producing high spatial resolution and hence realistic hydrodynamic representation of the local flow processes in the narrow interconnecting passages. In principle, the numerical modelling strategy could be utilized to assess the impact of natural or man-made changes to a typical connecting channel geometry. Although the results are preliminary, the case indicates the potential of quadtree-based meshes for application to complicated shallow flow geometries.

## 6. CONCLUSIONS

An explicit time stepping numerical model for the solution of the shallow water equations on hierarchical quadtree grids has been presented in this paper. Hierarchical grids are capable of

 

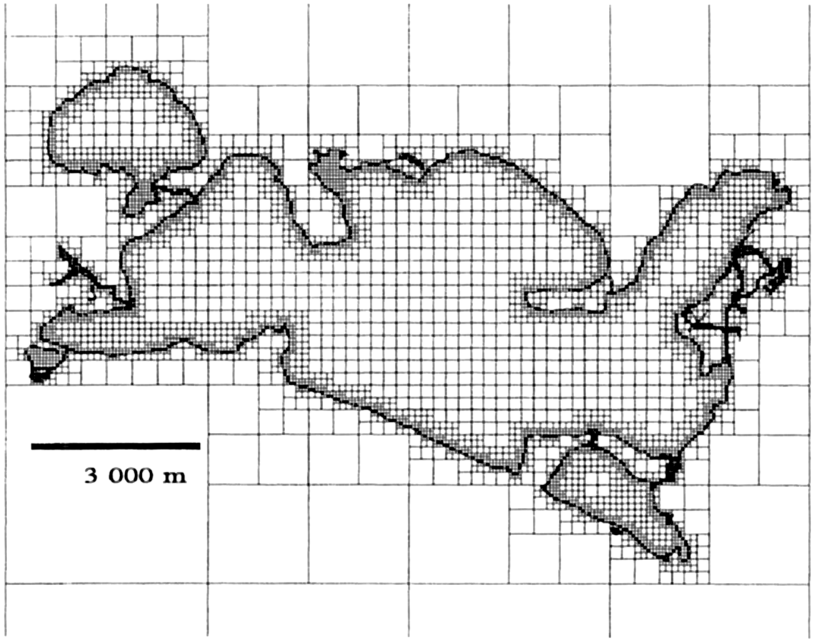


Figure 21. Regularized quadtree grid fitted to Nichupté Lagoon geometry.

spatially discretizing large flow domains while giving high resolution in sub-regions where, for example, the current shear or vorticity is greatest. In a fractal sense, quadtree grids can readily be fitted to any boundary no matter how distorted, provided absolute convergence to the boundary is not required and a low level of stepped boundary can be tolerated. Herein, a new quadtree numbering system is proposed whereby recursion is avoided and the indexing system corresponds to finite volume (or finite difference) notation, rendering neighbour cell finding straightforward. In the new numbering system each cell has three integer values, the first represents the position in the $x$-direction, the second the $y$-direction position, and the third is the subdivision level of the cell. It should be noted that quadtree grids are well suited to applications involving irregular boundaries, or where the flow contains locally steep velocity gradients; for nearly uniform domains, the cost of using a quadtree grid is likely to outweigh that of the equivalent uniform grid whether it be rectangular or curvilinear.

The unsteady shallow water equations are discretized using finite volumes on quadtree grids with a staggered arrangement of the water level and mass flux variables. Grid adaptation is according to a cell circulation parameter. A range of validation tests has been used to test the solver. The results for seiching without friction in a rectangular channel indicate that the model predicts the natural frequency of oscillation accurately, but produces slight dissipation of the standing wave. The Coriolis test demonstrates that the model correctly handles the appropriate source term. Laminar jet-forced flow in a circular basin has been modelled using adaptive

 

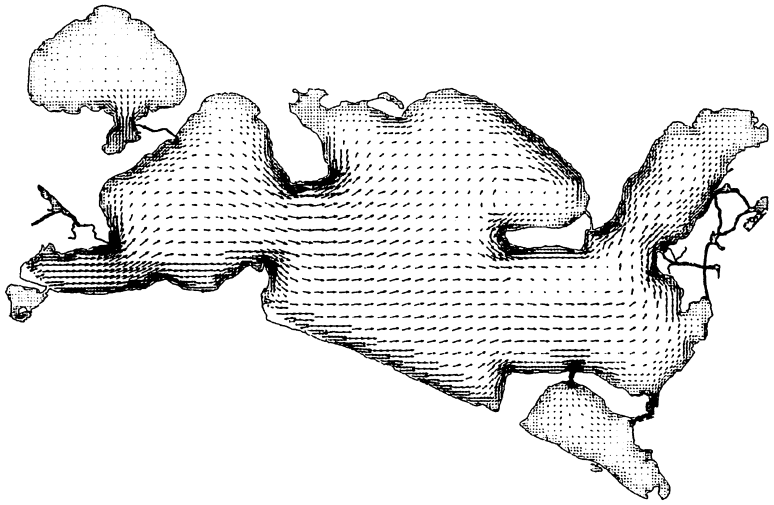

Figure 22. Simulated wind-induced flow in the Nichupté Lagoon.

quadtree grids, and the steady state flow pattern was found to be very similar to that found by alternative models (e.g. Dennis [34] and Borthwick and Kaar [13]). The model is able to predict the detailed localized growth of vortices either side of the throughflow stream, which jets from inlet to outlet. Wetting and drying at moving land water interfaces has been incorporated in the model. An illustrative example of the application of the quadtree based shallow flow solver to extremely complicated multi-connected regions is provided by wind-induced flow in the Nichupté Lagoon, México.

## ACKNOWLEDGMENTS

This work has been supported by the Mexican Government, the National Scientific Fund of Hungary through grant T017606, and the Hungarian–British Science and Technology Programme. The UK Engineering and Physical Sciences Research Council (EPSRC) is funding extensions of this work to species transport and coastal process modelling through grants GR/L11861 and GR/L92877.

## REFERENCES

1. Stansby PK, Lloyd P. A semi-implicit Lagrangian scheme for 3D shallow water flow with a two-layer turbulence model. *International Journal for Numerical Methods in Fluids* 1995; **20**: 115–133.
2. Falconer RA, Alstead RD. Computational flow modelling in coastal and estuarine waters using irregular grid schemes. SERC Report Ref. No. GR/E65197, 1990; 1–18.
3. Rodenhuis GS. Two-dimensional nearly-horizontal flow models. In *Coastal, Estuarial and Harbour Engineers' Reference Book*, Abbott MB, Price WA (eds). E & FN Spon: London, 1994; 129–144.
4. Butler HL. Coastal flood simulation in stretched coordinates. In *Proceedings of the 16th Coastal Engineering Conference*, ASCE, Hamburg, Germany, vol. 1, 1978; 1030–1048.

 

5. Johnson BH. VAHM—a vertically averaged hydrodynamic model using boundary-fitted coordinates. Misc. Paper HL-80-3, US Army Engineer Waterways Experiment Station Hydraulics Laboratory, Vicksburg, MI, USA, 1980.
6. Thompson JF, Warsi ZUA, Mastin CW. *Numerical Grid Generation: Foundations and Applications*. North-Holland Press: Amsterdam, 1985.
7. Willemse JBTM, Stelling GS, Verboom GK. Solving the shallow water equations with an orthogonal coordinate transformation. Presented at the International Symposium on Computational Fluid Dynamics, Tokyo [reprinted as Delft Hydraulics Communication No. 356, January 1986, Delft Hydraulics Laboratory, The Netherlands], 1985.
8. Lin BL, Falconer RA. Modelling sediment fluxes in estuarine waters using curvilinear coordinate system. *Estuarine Coastal and Shelf Science* 1995; **41**: 413–428.
9. Borthwick AGL, Barber RW. River and reservoir flow modelling using the transformed shallow water equations. *International Journal for Numerical Methods in Fluids* 1992; **14**: 1193–1217.
10. Ye J, McCorquodale JA. Depth-averaged hydrodynamic model in curvilinear collocated grid. *ASCE Journal of Hydraulic Engineering* 1997; **123**(5): 380–388.
11. Sheng YP, Hirsh JE. Numerical solution of shallow water equations in boundary-fitted grids. Technical Memo 84-15, Aeronautical Research Associates of Princeton, Inc., Princeton, NJ, USA, 1984.
12. Borthwick AGL, Akponasa GA. Reservoir flow prediction by contravariant shallow water equations. *ASCE Journal of Hydraulic Engineering* 1997; **123**(5): 432–439.
13. Borthwick AGL, Kaar ET. Shallow flow modelling using curvilinear depth-averaged stream function and vorticity transport equations. *International Journal for Numerical Methods in Fluids* 1993; **27**: 417–445.
14. Scott LJ, Barber RW. The effects of grid adaptation on tidal propagation in a boundary-fitted coordinate system. In *Proceedings of the 4th International Conference on Numerical Grid Generation in CFD*, Weatherill NP (ed.). Pineridge Press: Swansea, 1994; 603–614.
15. Thacker WC. Irregular grid finite-difference techniques: simulations of oscillations in shallow circular basins. *Journal of Physical Oceanography* 1977; **7**: 284–292.
16. Thacker WC. Some exact solutions to the non-linear shallow-water wave equations. *Journal of Fluid Mechanics* 1981; **107**: 499–508.
17. Bauer SW, Schmidt KD. Irregular-grid finite-difference simulation of Lake Geneva surge. *ASCE Journal of Hydraulic Engineering* 1983; **109**(10): 1285–1297.
18. Anastasiou K, Chan CT. Solution of the 2D shallow water equations using the finite volume method on unstructured triangular meshes. *International Journal for Numerical Methods in Fluids* 1997; **24**: 1225–1245.
19. Neta B. Analysis of finite elements and finite differences for shallow water equations. *Mathematics and Computers in Simulation* 1992; **34**: 141–161.
20. Kolar RL, Gray WG, Westerink JJ, Luettich RA. Shallow water modelling in spherical coordinates: equation formulation, numerical implementation, and application. *Journal of Hydraulic Research* 1994; **32**(1): 3–24.
21. Gáspár C, Józsa J, Sarkkula J. Shallow lake modelling using quadtree-based grids. In *Proceedings of the X International Conference on Computational Methods in Water Resources*, Heidelberg, Peters A (ed.). Kluwer: Amsterdam, 1994; 1053–1060.
22. Samet H. *The Design and Analysis of Spatial Data Structures*. Addison-Wesley: Reading, MA, 1990.
23. Samet H. Neighbour finding techniques for images represented by quadtrees. *Computer Graphics and Image Processing* 1982; **18**: 37–57.
24. Baehmann PL, Wittchen SL, Shephard MS, Grice KR, Yerry MA. Robust, geometrically based, automatic two-dimensional grid generation. *International Journal for Numerical Methods in Engineering* 1987; **24**: 1043–1078.
25. Cheng JH, Finnigan PM, Hathaway AF, Kela A, Schroeder WJ. Quadtree/octree meshing with adaptive analysis. In *Numerical Grid Generation in CFD*, Sengupta S (ed.). Pineridge Press: Swansea, 1988; 633–642.
26. Van Dommelen L, Rundensteiner EA. Fast, adaptive summation of point forces in the two-dimensional Poisson equation. *Journal of Computational Physics* 1989; **83**: 126–147.
27. Greaves DM, Borthwick AGL. On the use of adaptive hierarchical meshes for numerical simulation of separated flows. *International Journal for Numerical Methods in Fluids* 1998; **26**: 303–322.
28. Gáspár C, Józsa J, Simbierowicz P. Lagrangian modelling of the convective-diffusion problem using unstructured grids and multigrid technique. In *Proceedings of the 1st International Conference on Water Pollution (Modelling, Measuring and Prediction)*, 3–5 September, Southampton, UK, Wrobel LC, Brebbia CA (eds). Computational Mechanics: Southampton, 1991.
29. Józsa J, Gáspár C. Fast, adaptive approximation of wind-induced horizontal flow patterns in shallow lakes using quadtree-based multigrid method. In *Proceedings of the IX International Conference on Computational Methods in Water Resources*, 9–11 June, Denver, CO, USA, Russell TF (ed.). Computational Mechanics: Southampton, 1992.
30. Edwards GE. Elimination of adaptive grid interface errors in the discrete cell centred pressure equation. *Journal of Computational Physics* 1996; **126**: 356–372.

 

31. Falconer RA. An introduction to nearly-horizontal flows. Chapter 2. In *Coastal, Estuarial and Harbour Engineers' Reference Book*, Abbott MB, Price WA (eds). E & FN Spon: London, 1994; 27–36.
32. Van der Maarel HTM. A local grid refinement method for the Euler equations. PhD thesis, Amsterdam University, The Netherlands, 1993.
33. Koren B. A robust upwind discretisation method for advection, diffusion and source terms. In *Numerical Methods for Advection–Diffusion Problems*, *Notes on Numerical Fluid Mechanics*, vol. 45, Vreugdenhil CB, Koren B (eds). Vieweg: Wiesbaden, 1993; 117–137.
34. Fraccorollo L, Toro EF. Experimental and numerical assessment of the shallow water model for two-dimensional dam-break type problems. *Journal of Hydraulic Research* 1995; **33**(6): 843–863.
35. Cruz León S. Numerical solution of the shallow water equations on quadtree grids. DPhil thesis, Oxford University, UK, 1997.
36. Falconer RA, Owens PH. Numerical simulation of flooding and drying in a depth-averaged tidal flow model. *Proceedings of the Institution of Civil Engineers*, *Part 2* 1987; **83**: 161–180.
37. Falconer RA, Chen Y. An improved representation of flooding and drying and wind stress effects in a two-dimensional tidal numerical model. *Proceedings of the Institution of Civil Engineers*, *Part 2* 1991; **91**: 659–678.
38. Dennis SCR. Application of the series truncation method to two-dimensional internal flows. In *Proceedings of the 4th International Conference on Numerical Methods in Fluid Dynamics*, Colorado, Richtmyer RD (ed.). Springer: New York, 1974; 146–151.

 